Nanoscale

PAPER

View Article Online
View Journal | View Issue

Cite this: *Nanoscale*, 2016, **8**, 5649

Nacre-inspired integrated strong and tough reduced graphene oxide–poly(acrylic acid) nanocomposites

Sijie Wan,†[a] Han Hu,†[a] Jingsong Peng,†[a] Yuchen Li,†[b] Yuzun Fan,[a] Lei Jiang[a] and Qunfeng Cheng*[a,c]

Received 21st January 2016,
Accepted 2nd February 2016

DOI: 10.1039/c6nr00562d

www.rsc.org/nanoscale

Inspired by the relationship between interface interactions and the high performance mechanical properties of nacre, a strong and tough nacre-inspired nanocomposite was demonstrated based on graphene oxide (GO) and polyacrylic acid (PAA) prepared *via* a vacuum-assisted filtration self-assembly process. The abundant hydrogen bonding between GO and PAA results in both high strength and toughness of the bioinspired nanocomposites, which are 2 and 3.3 times higher than that of pure reduced GO film, respectively. In addition, the effect of environmental relative humidity on the mechanical properties of bioinspired nanocomposites is also investigated, and is consistent with previous theoretical predictions. Moreover, this nacre-inspired nanocomposite also displays high electrical conductivity of 108.9 S cm^{-1}. These excellent physical properties allow this type of nacre-inspired nanocomposite to be used in many applications, such as flexible electrodes, aerospace applications, and artificial muscles *etc.* This nacre-inspired strategy also opens an avenue for constructing integrated high performance graphene-based nanocomposites in the near future.

With the rapid development of flexible electrical devices, multifunctional and highly conductive graphene films are needed.[1] However, pure chemically reduced graphene films are brittle with low strain at break. Blending with polymers by methods used for traditional composites can only slightly improve the mechanical properties, however, it usually greatly decreases the composites' electrical conductivities due to the low content of graphene in the resultant composites. Recently, graphene oxide (GO), a derivative of graphene, possessing excellent mechanical properties, has become an ideal candidate for assembling high performance graphene-based nanocomposites[2–4] due to their abundant functional groups.[5] Many GO-based layered materials have been reported, such as PVA reinforced GO nanocomposites,[6,7] metal ion cross-linked GO materials,[8] borate covalently cross-linked GO materials (GO–borate),[9] GO materials covalently cross-linked with small molecules of glutaraldehyde (GA),[10] GO materials covalently cross-linked with long molecules of polyallylamine,[11] and polyetherimide (PEI) covalently cross-linked GO materials (GO–PEI).[12] However, the aforementioned GO-based materials demonstrate superior properties in only one physical property, such as high tensile strength, stiffness or toughness. It remains a great challenge to construct both strong and tough graphene-based nanocomposites.

Nacre, the 'gold standard' for biomimicry with both high strength and toughness after billions of years of evolution,[13] has been a source of inspiration in the design of hybrid materials and nanocomposites.[5,14–16] The unique structure of nacre shows a "bricks and mortar" layered architecture alternatively packed with 95 vol% of two-dimensional (2D) aragonite calcium carbonate platelets, and 5 vol% of one-dimensional (1D) nanofibrillar chitin and protein with excellent interface interactions.[13]

Herein, inspired by the relationship between nacre's unique structure and outstanding mechanical properties, we fabricated strong, tough and conductive nanocomposites based on graphene oxide (GO) and poly(acrylic acid) (PAA) *via* hydrogen bonding. The tensile strength and toughness were simultaneously improved to 2 and 3.3 times higher than that of pure reduced GO film, respectively. Moreover, this nacre-inspired nanocomposite (rGO–PAA) shows high electrical conductivity, which is attractive for potential applications in flexible electrical electrodes, aerospace applications, and artificial muscles

[a]*Key Laboratory of Bio-inspired Smart Interfacial Science and Technology of Ministry of Education, School of Chemistry Environment, BeiHang University, Beijing, 100191, P. R. China. E-mail: cheng@buaa.edu.cn*
[b]*Beijing Engineering Research Center of Printed Electronics, Beijing Institute of Graphic Communication, Beijing 102600, P. R. China*
[c]*State Key Laboratory for Modification of Chemical Fibers and Polymer Materials, Donghua University, Shanghai 201620, P. R. China*
†These authors contributed equally to this work.

etc. In addition, the effect of environmental relative humidity (RH) is also investigated, which is well consistent with the previous simulation prediction. This nacre-inspired strategy opens an avenue for the construction of high performance graphene-based nanocomposites in the future.

The preparation process for the nacre-inspired nanocomposite is illustrated in Fig. 1a. Firstly, exfoliated GO sheets were dispersed into the deionized (DI) water and subsequently mixed with PAA solution to form homogeneous solution. GO sheets were obtained *via* a modified hummers' method with a size and thickness of 0.2–0.8 μm and 0.75 nm, respectively, which were characterized by atomic force microscopy (AFM) (Fig. S1†). Then, the mixture of GO/PAA solution was filtered by vacuum-assisted filtration and assembled into GO–PAA nanocomposites. Finally, the GO–PAA nanocomposite was chemically reduced by hydroiodic acid (HI) to recover the conjugated structure of the graphitic lattice. The rGO–PAA nacre-inspired nanocomposites were obtained, and a digital photograph is shown in Fig. 1b.

To investigate the effect of PAA content on the mechanical properties of nanocomposites, four kinds of GO–PAA nanocomposites with different GO contents have been fabricated, which were designated as GO–PAA-I, GO–PAA-II, GO–PAA-III, and GO–PAA-IV, respectively. The exact GO contents were determined by thermogravimetric analysis (TGA), as listed in Table 1. The corresponding TGA curves are shown in Fig. S2.† The cross-section of the resultant rGO–PAA-IV nanocomposites present a typical layered structure similar to natural nacre, observed from the scanning electron microscopy (SEM) images in Fig. 1c and d. The cross-section SEM images of other GO–PAA and rGO–PAA nanocomposites are also shown in Fig. S3 and S4.† The layered structure was also confirmed by X-ray diffraction (XRD), as shown in Fig. 2a and S5.† An apparent strong 002 reflection was observed in all GO–PAA (10.0°–11.5°) and rGO–PAA (22.0°–24.0°) nanocomposites. The calculated interlayer distance (*d*-spacing) from XRD characterization was

Table 1 GO content and the electrical conductivity after HI reduction of GO and GO–PAA nanocomposites

Sample	Input GO content (wt%)	GO content by TGA (wt%)	Electrical conductivity after HI reduction (S cm^{-1})
GO	—	—	124.2 ± 9.2
GO–PAA-I	50	55.65	54.2 ± 8.1
GO–PAA-II	70	71.97	77.2 ± 6.4
GO–PAA-III	90	92.06	95.5 ± 7.7
GO–PAA-IV	95	95.49	108.9 ± 7.4

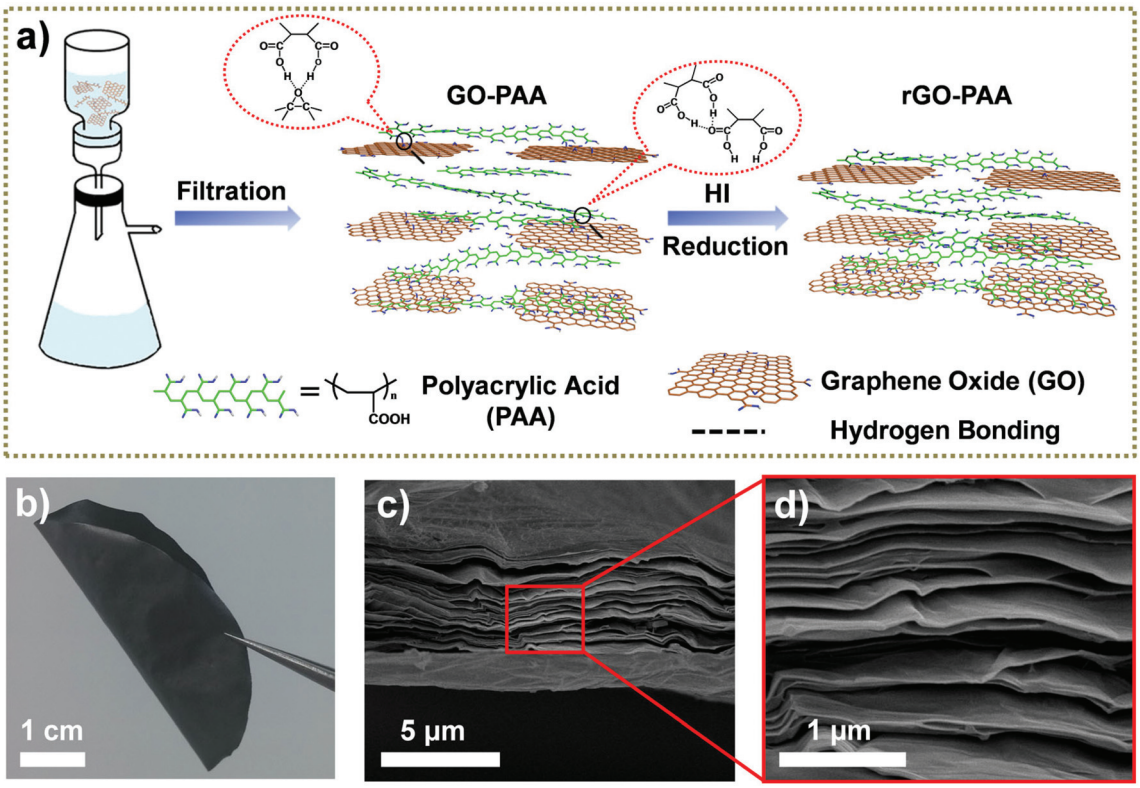

Fig. 1 Illustration of the fabrication process of the rGO–PAA nanocomposites. (a) The GO nanosheets/PAA homogeneous solution was filtered by vacuum-assisted filtration into GO–PAA nanocomposites. Then after HI reduction, the rGO–PAA nanocomposites were obtained. (b) A digital photograph of rGO–PAA nanocomposites. (c) and (d) The cross-section surface morphology with different magnifications of rGO–PAA-IV nanocomposites.

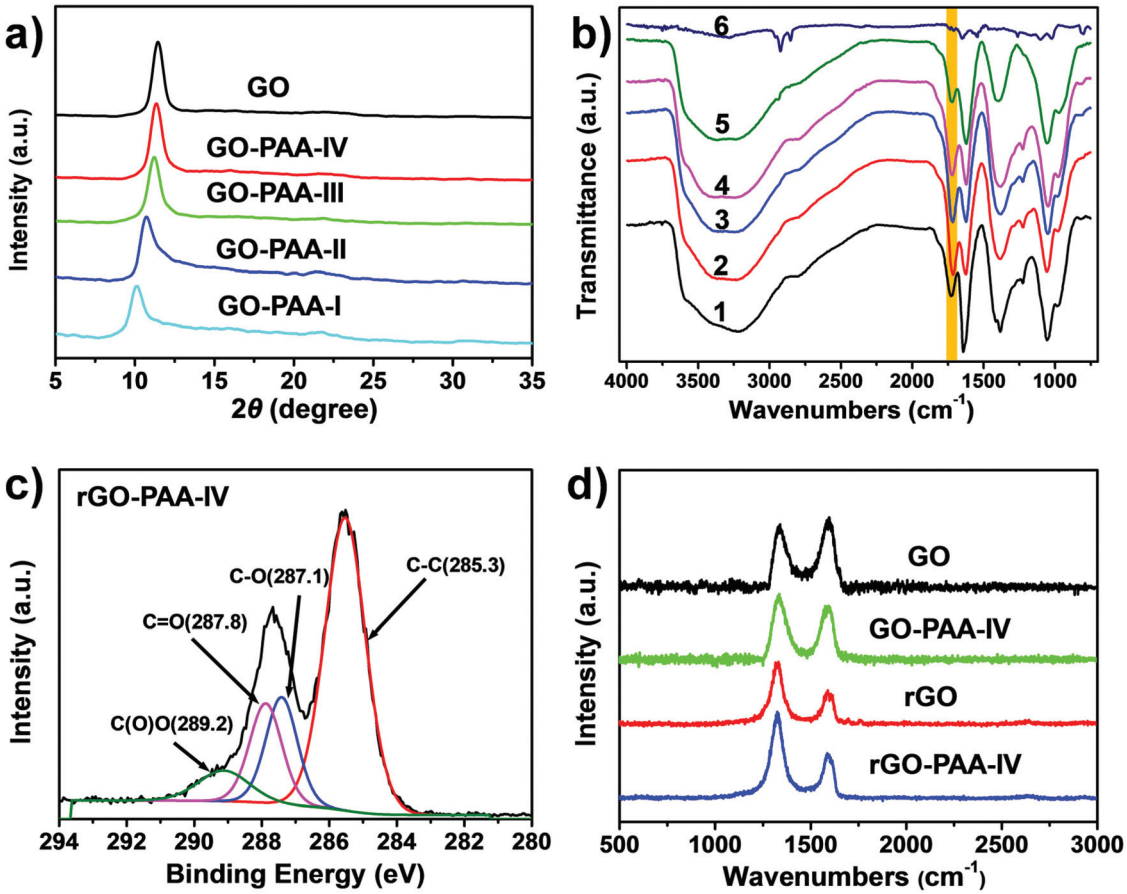

Fig. 2 Characterization comparison of GO, rGO films and nacre-inspired nanocomposites. (a) XRD patterns of pure GO film and GO–PAA nanocomposites. (b) The FTIR spectra of pure GO (curve 1) film, GO–PAA I-IV (curves 2–5) nanocomposites and pure PAA (curve 6) film. The gradual red-shift from 1728 cm^{-1} for pure GO film to 1716 cm^{-1} for GO–PAA-I nanocomposite demonstrates the hydrogen bonding between GO and PAA. (c) The XPS spectrum of the rGO–PAA-IV nanocomposite. The C_{1s} broad peak could be fitted into four peaks at 285.3 eV, 287.1 eV, 287.8 eV and 289.2 eV corresponding to C–C, C–O, C=O and C(O)O, respectively. (d) The Raman spectra of pure GO and rGO films, GO–PAA-IV and the rGO–PAA-IV nanocomposite. The I_D/I_G ratio increased from 0.86 for pure GO film and 1.29 for the GO–PAA-IV composite to 2.28 for rGO film and 2.39 for the rGO–PAA-IV nanocomposite, respectively. These results also show that the sp^2 hybridized carbons were restored after HI reduction.

listed in Table S2.† With increasing PAA content, the *d*-spacing increased to 8.82 Å for GO–PAA-I from 7.70 Å for pure GO film, indicating that the PAA molecule was successfully embedded into the gallery between adjacent GO sheets. Fourier transform infrared spectroscopy (FTIR) was conducted, as shown in Fig. 2b. The C=O stretching vibration bands in the carboxyl groups of GO were observed at 1728 cm^{-1} (curve 1), while that of the PAA molecule was located at 1710 cm^{-1} (curve 6). With increasing PAA content, the C=O vibration band of GO–PAA nanocomposites was gradually red-shifted to 1716 cm^{-1} (curves 2–5), which indicated the extensive hydrogen bonding between GO and PAA.[17] Similar red-shifting of the C=O vibration band could also be observed from the FTIR of rGO–PAA nanocomposites, as shown in Fig. S6,† indicating the hydrogen bonding remains after HI reduction.

X-ray photoelectron spectroscopy (XPS) was performed, as shown in Fig. 2c and S7.† The relative peak intensity of C–O and C=O groups of pure GO film is also substantially decreased after HI reduction. The atomic ratio of O_{1s} to C_{1s} for both pure rGO film and the rGO–PAA-IV nanocomposite is much lower than that of pure GO film and the GO–PAA-IV nanocomposite, as listed in Table S3,† indicating effective elimination of oxygen-containing functional groups and partial recovery of graphitic conjugated hexagonal network after HI reduction.[18] Compared with GO–PAA-IV (Fig. S7c†), the rGO–PAA-IV nanocomposite shows a significant decrease of relative intensity of the signals from the C–O groups (Fig. 2c). Raman spectra (Fig. 2d) demonstrate that the relative peak intensity ratio of the D band to the G band (I_D/I_G) increased from 1.29 for the GO–PAA-IV nanocomposite to 2.39 for the rGO–PAA-IV nanocomposite, as listed in Table S3,† further verifying the restoration and homogenization of sp^2 hybridized carbons after HI reduction.[19] The elimination of oxygen-containing functional groups would decrease the interlayer distance of adajcent rGO sheets, as shown in Table S2,† which effectively increases the friction and π–π conjugated interaction between adjacent rGO sheets,[20] and

further improves the mechanical properties of rGO–PAA nanocomposites.

The typical tensile stress–strain curves of GO–PAA and rGO–PAA nanocomposites are shown in Fig. 3a. The pure GO film possesses a tensile strength of 99.18 ± 2.31 MPa and toughness of 1.17 ± 0.17 MJ m^{-3}, consistent with previous reports.[21] After HI reduction, the tensile strength and toughness of rGO film is improved to 157.27 ± 7.81 MPa and 2.69 ± 0.06 MJ m^{-3}, respectively. This improvement should be attributed to the increased friction and π–π conjugated interaction between adjacent rGO sheets with decreased *d*-spacing.[18] Owing to the abundant hydrogen bonding, the GO–PAA-IV nanocomposite shows a simultaneously enhanced tensile strength of 206.12 ± 4.79 MPa and toughness of 3.78 ± 0.31 MJ m^{-3}, respectively. After HI reduction, the hydrogen bonding could be decreased to a certain extent due to removal of these functional groups on GO surface, while the friction and π–π conjugated interaction between adjacent rGO sheets would be significantly increased because of the decreased *d*-spacing and paitial recovery of rGO conjugated structure. Therefore, similar to rGO film, the tensile strength and toughness of the rGO–PAA-IV nanocomposite, with respect to GO–PAA-IV, is further increased to 309.57 ± 27.00 MPa and 8.88 ± 1.13 MJ m^{-3}, which is 3.1 and 7.6 times higher than that of pure GO film, respectively. The tensile strength and toughness of rGO–PAA nanocomposites with different GO content are shown in Fig. 3b and c, respectively. With the GO content increasing, the tensile strength and toughness of nanocomposites reach peak value at the GO content of 95.49 wt%. In this work, the optimal PAA content is determined to be 4.51 wt%, corresponding to the rGO–PAA-IV nanocomposite. Compared with pure rGO film, the tensile strength and toughness of the rGO–PAA-IV nanocomposite is enhanced simultaneously by 2 times and 3.3 times, respectively, which should be attributed to the hydrogen bonding network between the rGO sheets and PAA molecule chains. However, the excess PAA would just act as an impurity to increase the cross-sectional area of the rGO–PAA nanocomposites, the mechanical properties decrease with further addition of PAA. This phenomenon is consistent with inorganic nanofiller loading (95 vol%) in natural nacre, further embodying the advantage of the nacre-mimicking strategy. A similar trend was also found in the GO–PAA nanocomposites as shown in Fig. S8.† The detailed mechanical properties are listed in Table S4.†

To understand the high mechanical properties of the rGO–PAA-IV nanocomposite, the proposed fracture mode is illustrated in Fig. 3d. HI reduction definitely would remove the functional groups on the GO sheets to a certain extent, however, hydrogen bonding formed between the hydroxyl and carbonyl groups on the GO sheets and carbonyl groups on PAA

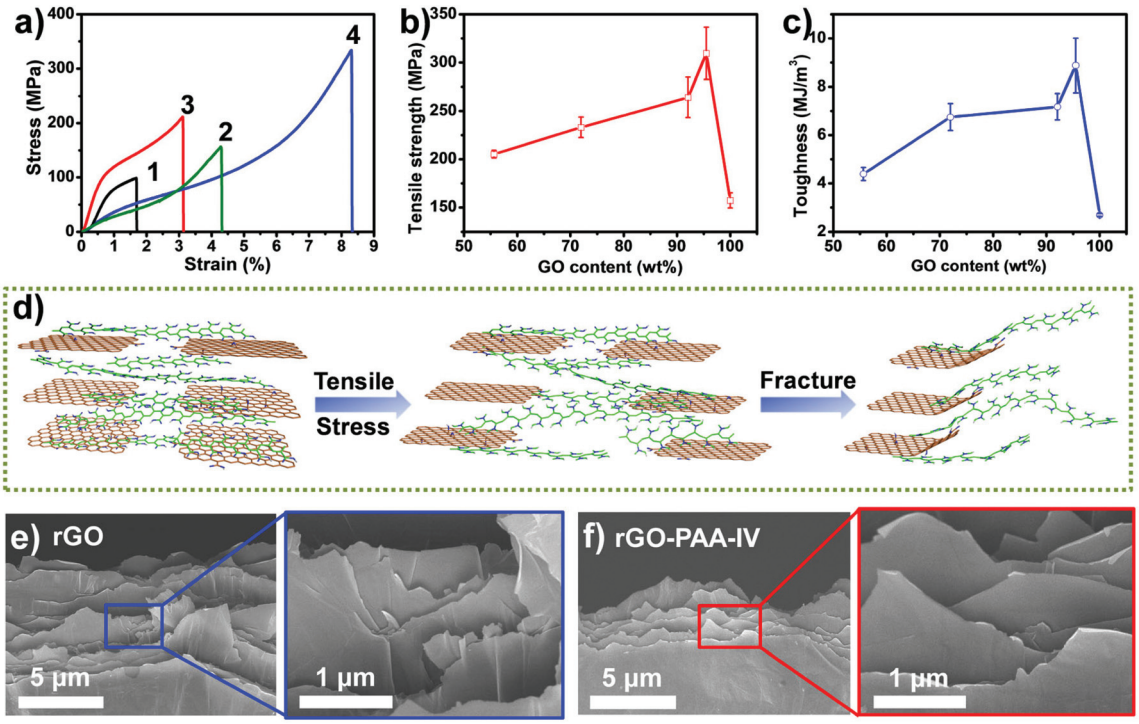

Fig. 3 Mechanical properties of nacre-inspired nanocomposites. (a) The typical tensile stress–strain curves of pure GO film (curve 1), pure rGO film (curve 2), GO–PAA-IV (curve 3) and rGO–PAA-IV (curve 4) nanocomposites. The tensile strength (b) and toughness (c) comparison of rGO–PAA nanocomposites with different GO content. (d) The proposed fracture mode of rGO–PAA-IV nanocomposites. The side view of a cross-section of the fracture surface morphology of pure rGO film (e) and the rGO–PAA-IV nanocomposite (f). The pure rGO film displays brittle fracture morphology with only rGO sheets pulled out while the rGO sheets of rGO–PAA-IV nanocomposites are not only pulled out but much more curved due to the fracture of the extra hydrogen bonding network between PAA and GO.

would be sustained in the process of HI reduction, which can be confirmed by FTIR, as shown in Fig. S6.† Thus, upon stressing, the hydrogen bonding first causes fracture, triggering the slippage of adjacent rGO sheets. With gradually increased loading, due to the continuous breakage and recreation of hydrogen bonding,[6,22,23] the PAA molecule chain would be stretched successively from a coiled to straight conformation, resulting in large strain and dissipation of much more energy. When the load was further increased, the hydrogen bonding was sufficiently destroyed, and the friction and π–π conjugated interaction between adjacent rGO sheets also absorbed an amount of energy. Finally, the rGO–PAA nanocomposites fractured. Due to the slippage of adjacent rGO sheets resulting from the fracture of π–π conjugated interaction, the fracture morphology of pure rGO film shows the pulled out of rGO sheets (Fig. 3e). Compared to the pure rGO film, the rGO sheets of rGO–PAA-IV nanocomposite are not only pulled out but much more curled, on account of the fracture of extra hydrogen bonding network between the rGO sheets and PAA molecule chains, as shown in Fig. 3e and f. The side view of the cross-section of other GO–PAA and rGO–PAA nanocompsites are shown in Fig. S3 and S4.†

It is well known that the water content has a great effect on the hydrogen bonding and further effect on the mechanical properties of GO-based nanocomposites.[23] Under an atmospheric temperature of 25 °C, the environmental relative humidity (RH) is about 16% RH. A series of RHs, such as 40%, 60%, 80% and 100%, can be obtained through tuning environmental conditions. The mechanical properties of nacre-inspired nanocomposites under different RHs were tested, including tensile strength, Young's modulus, elongation at break, and toughness. Fig. 4 shows the mechanical properties of nacre-inspired nanocomposites with different environmental relative humidities. Both tensile strength and Young's modulus of pure GO and rGO films, GO–PAA-IV and rGO–PAA-IV nanocomposites decreased with increasing environmental RH, while the corresponding strain was increased with increasing environmental RH. Based on the previous reported results from theoretical simulations and experimental analysis on the modulus of GO film and GO–PVA nanocomposite,[23] the optimal water content was determined to be ~5 wt%, and further increasing the water content would decrease the modulus of both GO film and the GO–PVA nanocomposites. In this work, the water content of pure GO film and the GO–PAA-IV nanocomposite with an environmental RH of 16% are calculated by TGA to be about 4.26 wt% and 5.92 wt%, respectively. Our experimental results are consistent with the previous theoretical simulation.[23] The main reason for this phenom-

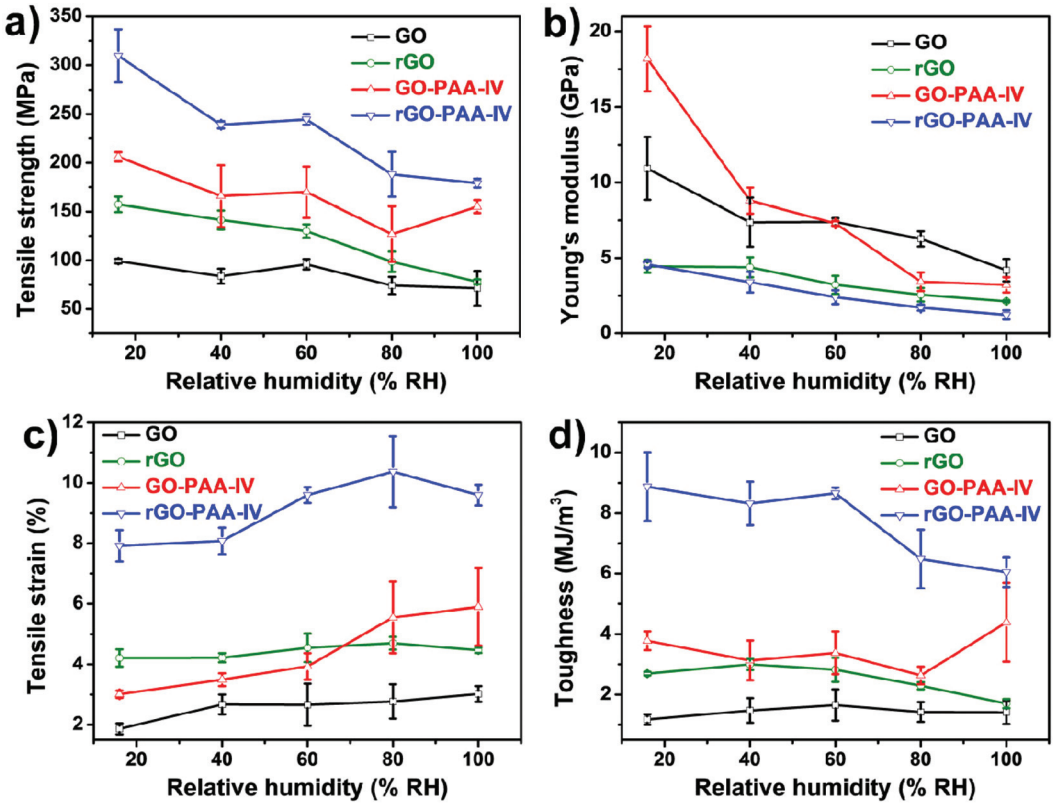

Fig. 4 The effect of environmental relative humidity on the mechanical properties of pure GO and rGO films, GO–PAA-IV and rGO–PAA-IV nanocomposites: (a) tensile strength, (b) Young's modulus, (c) tensile strain and (d) toughness. The tensile strength and Young's modulus of these materials decreased with increasing environmental relative humidity, while the tensile strain increased with increasing environmental relative humidity. These experimental results are consistent with the theoretical prediction by simulation.[23]

enon could be explained as follows: for pure GO and rGO films, the water would only increase the hydrogen bonding between the water molecules, which do not bridge adjacent graphene sheets, and swell the structure, facilitating lateral slippage of adjacent graphene sheets. On the other hand, excess water within a nacre-inspired nanocomposite structure would promote water–PAA, water–graphene sheets and water–water hydrogen bonding, which serve as the lubricant between adjacent graphene sheets. Thus, although the strain shows a little bit of increase, the toughness of the resultant nacre-inspired nanocomposites, calculated by integrating the stress–strain curve, shows no obvious correlation with the environmental relative humidity. The tensile stress–strain curves of pure GO and rGO films, GO–PAA-IV and rGO–PAA-IV nanocomposites under different environmental relative humidities are shown in Fig. S9,† and the corresponding detailed mechanical properties are listed in Table S5.†

Compared with natural nacre and other GO-based nacre-inspired modified materials, the rGO–PAA-IV nanocomposite possessed integrated high mechanical properties, as shown in Fig. 5 and the detailed mechanical properties are listed in Table S6.† Most GO-based layered materials often present high tensile strength or stiffness but relatively low toughness. For example, GO–borate materials with covalent cross-linking of small molecule borate possess remarkable stiffness up to 127 ± 4 GPa, but low toughness of 0.14 MJ m^{-3},[9] which is much lower than that of natural nacre.[13] Moreover, the GO–PEI nanocomposites with high tensile strength were constructed based on PEI cross-linked GO sheets.[12] The tensile strength is as high as 209.9 MPa, however, the toughness is only 0.23 MJ m^{-3}. The low toughness could also be found in the GO–GA[10] and rGO–SL[24] layered materials, which might be due to the strong interface interaction restricting the slippage of GO sheets when loading. While for the rGO–PAA-IV nanocomposite, the hydrogen bonding not only improves the tensile strength, but also allows the continuous slippage of rGO sheets and coiled PAA molecule chains stretching, resulting in high toughness through breakage and recreation of hydrogen bonding.[6,22,23]

The toughness of the rGO–PAA-IV nanocomposite is 3, 29, 38 and 63 times higher than that of rGO–SL,[24] GO–GA,[10] GO–PEI,[12] and GO–borate,[9] composites, respectively. In comparison with GO–PMMA,[6] and rGO–PVA[7] composites with interface interactions of hydrogen bonding, the strength and toughness of rGO–PAA-IV nanocomposites is also superior, which is due to relatively more abundant hydrogen bonding. In addition, the integrated mechanical properties of rGO–PAA-IV nanocomposites with hydrogen bonding are also superior to other GO-based nanocomposites with other interface interactions, including ionic bonding, π–π interactions, and covalent bonding. For example, the tensile strength and toughness of the rGO–PAA-IV nanocomposite are 2.4 and 28 times higher than that of GO–Ca^{2+},[8] and 3.8 and 68 times higher than that of GO–Mg^{2+},[8] respectively. The polyallylamine covalently cross-linked GO film[11] shows a strength of 91.9 MPa and toughness of 0.15 MJ m^{-3}, which is only one third and one sixtieth than that of the rGO–PAA-IV nanocomposite, respectively. Moreover, this nacre-inspired nanocomposite is superior to GO-based nanocomposites with covalent bonding, such as rGO–PCDO,[21] and rGO–PDA.[20] Recently, some integrated GO-based nanocomposites have also been constructed through synergistic interface interactions, such as rGO–PAPB,[25] rGO–CS,[26] and rGO–CNC.[27] Although the tensile strength of the rGO–PAA-IV nanocomposite is slightly lower than that of these materials, the toughness of rGO–PAA-IV is excellent, which is 1.2 times and 4.9 times higher than that of rGO–PAPB and rGO–CNC, respectively. Due to the absence of covalent bonding, the strength and toughness of rGO–PAA-IV is lower than that of rGO–CS through synergistic interface interactions of covalent and hydrogen bonding. Meanwhile, the rGO–PAA-IV nanocomposites are superior to the ternary rGO–MoS_2–TPU nanocomposite[28] with tensile strength of 235.3 ± 19.4 MPa and toughness of 6.9 ± 0.5 MJ m^{-3} and comparable to the ternary rGO–DWNT–PCDO nanocomposite[29] with a tensile strength of 374.1 ± 22.8 MPa and toughness of 9.2 ± 0.8 MJ m^{-3}.

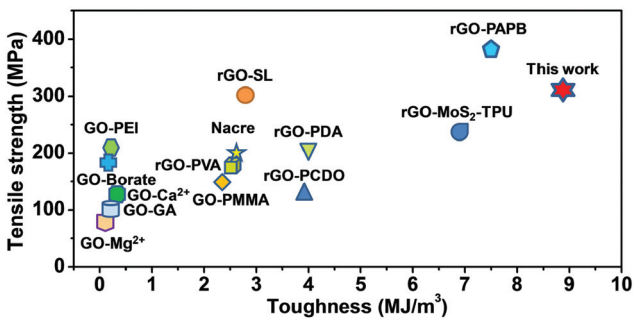

Fig. 5 Mechanical properties comparison of rGO–PAA nacre-inspired nanocomposites with nacre and other GO-based nanocomposites.

In addition to the excellent integrated high strength and toughness, the nacre-inspired rGO–PAA-IV nanocomposites are also attractive for providing excellent electrical conductivity after HI reduction. The rGO–PAA-IV nanocompsites show electrical conductivity of 108.88 S cm^{-1} (Table 1), superior to that of previous rGO–PVA[7] and rGO–PDA[20] nanocomposites. This unique combination of high strength, toughness and electrical conductivity would enable this nacre-inspired nanocomposites to be applied in flexible and wearable electronic devices.

In conclusion, inspired by natural nacre, we successfully constructed strong and tough rGO–PAA nanocomposites *via* hydrogen bonding. In addition, the relationship between the mechanical properties of rGO–PAA nanocomposites and environmental relative humidity have been also successfully experimentally demonstrated, and this is consistent with previous theoretical predictions. Moreover, the nacre-inspired nanocomposites also show attractively high electrical conductivity. These unique nacre-inspired nanocomposites could be great candidates for applications in flexible electrodes of supercapacitor, aerospace applications, artificial muscles, *etc*. This nacre-inspired strategy also creates a promising avenue

for constructing robust and highly conductive GO-based nanocomposites with integration of high strength and outstanding toughness in the near future.

Experimental section

Materials

Graphene oxide(GO) sheets were synthesized by modified Hummer's method and dried at 60 °C for storage following experiments. Polyacrylic acid (PAA, M_w = 3000) was purchased from Aladdin. The density of the PAA is about 1.23 g mL^{-1}. 57 wt% hydroiodic acid (HI) was purchased from Sigma-Aldrich. All the chemicals were used as received without further purification.

Fabrication of rGO–PAA nanocomposites

As-prepared GO sheets were dispersed into deionized water by stirring (2 h) and using sonification (30 min), to provide a homogeneous dispersion with a concentration of 1 mg mL^{-1}. Pure PAA liquid was diluted with deionized water at a concentration of 0.5 mg mL^{-1}. Then, a certain amount of PAA aqueous solution was added dropwise into the GO dispersion and stirred for 4 h and sonicated for 10 min to obtain a brown transparent solution without aggregation. Subsequently, the solution was assembled into a free-standing GO–PAA nanocomposite film through vacuum assisted filtration, followed by drying at 60 °C for 12 h and peeling off the filter membrane. In our experiment, four kinds of GO–PAA nanocomposites were fabricated with different GO contents, which were designated as GO–PAA-I, GO–PAA-II, GO–PAA-III, GO–PAA-IV. Finally, the resultant GO–PAA nanocomposites were immersed into HI solution for 6 h and chemically reduced to rGO–PAA nanocomposites.

Environmental relative humidity

In order to create a stable relative humidity environment, we designed a special device using a small foam box and an air humidifier which were connected by a rubber tube. The real-time relative humidity in the foam box could be read from a thermo-hygrometer pre-placed in the box. When humidifying, the water vapor was blown from the air humidifier to the foam box through the rubber tube. Relative humidity can be easily and stably controlled to the designed level by adjusting the power of the air humidifier. Herein, five environmental relative humidities were chosen: 16% RH (natural environmental humidity), 40% RH, 60% RH, 80% RH and 100% RH under a constant temperature of 25 °C. Under each environmental relative humidity, several sample strips with a length of 10 mm and width of 3 mm for each material were put into the small foam box and humidified for 10 min, resulting in enough humidity for the next tensile testing. Then the humidification processed samples were taken out from the box and immediately tested for mechanical properties characterization.

Characterization

Mechanical properties were characterised by a Shimadzu AGS-X Tester with a loading rate of 1 mm min^{-1}. The samples were cut into strips with a length of 10 mm and width of 3 mm and the results for each samples were obtained by averaging 3–5 specimens. Thermogravimetric analysis (TGA) was carried out in a TG/DTA6300, NSK with a temperature rising rate of 10 K min^{-1} under nitrogen. Scanning electron microscopy (SEM) images were recorded using a field-emission scanning electron microscope (JEOL-7500F). Atomic force microscopy (AFM) was performed using a Leica TCS SP5. Raman spectroscopy measurements were conducted using LabRAM HR800 (Horiba JobinYvon) with an excitation energy of 1.96 eV (633 nm). X-ray photoelectron spectroscopy (XPS) measurements were performed on an ESCALab220i-XL (ThermoScientific) using a monochromatic Al-Kα X-ray source. X-ray diffraction (XRD) profiles were obtained with Cu-Kα radiation (λ = 1.54 nm). FTIR spectra were recorded using a Thermo Nicolet nexus-470 FTIR instrument. The electrical conductivities were tested by a standard two-probe method using a source meter (Agilent E4980A).

Acknowledgements

This work was supported by the Excellent Young Scientist Foundation of NSFC (51522301), the National Natural Science Foundation of China (21273017, 51103004), Program for New Century Excellent Talents in University (NCET-12-0034), Beijing Nova Program (Z121103002512020), Fok Ying-Tong Education Foundation (141045), Open Project of Beijing National Laboratory for Molecular Sciences, the 111 Project (B14009), Aeronautical Science Foundation of China (20145251035, 2015ZF21009), State Key Laboratory for Modification of Chemical Fibers and Polymer Materials, Donghua University (LK1508), and the Fundamental Research Funds for the Central Universities (YWF-15-HHXY-001).

References

1 X. Wang and G. Shi, *Environ. Eng. Sci.*, 2015, **8**, 790–823.
2 K. Hu, D. D. Kulkarni, I. Choi and V. V. Tsukruk, *Prog. Polym. Sci.*, 2014, **39**, 1934–1972.
3 X. Huang, X. Qi, F. Boey and H. Zhang, *Chem. Soc. Rev.*, 2012, **41**, 666.
4 M. K. Liu, Y. E. Miao, C. Zhang, W. W. Tjiu, Z. B. Yang, H. S. Peng and T. X. Liu, *Nanoscale*, 2013, **5**, 7312–7320.
5 Q. Cheng, L. Jiang and Z. Tang, *Acc. Chem. Res.*, 2014, **47**, 1256–1266.
6 K. W. Putz, O. C. Compton, M. J. Palmeri, S. T. Nguyen and L. C. Brinson, *Adv. Funct. Mater.*, 2010, **20**, 3322–3329.
7 Y.-Q. Li, T. Yu, T.-Y. Yang, L.-X. Zheng and K. Liao, *Adv. Mater.*, 2012, **24**, 3426–3431.
8 S. Park, K.-S. Lee, G. Bozoklu, W. Cai, S. T. Nguyen and R. S. Ruoff, *ACS Nano*, 2008, **2**, 572–578.

9 Z. An, O. C. Compton, K. W. Putz, L. C. Brinson and S. T. Nguyen, *Adv. Mater.*, 2011, **23**, 3842–3846.
10 Y. Gao, L.-Q. Liu, S.-Z. Zu, K. Peng, D. Zhou, B.-H. Han and Z. Zhang, *ACS Nano*, 2011, **5**, 2134–2141.
11 S. Park, D. A. Dikin, S. T. Nguyen and R. S. Ruoff, *J. Phys. Chem. C*, 2009, **113**, 15801–15804.
12 Y. Tian, Y. Cao, Y. Wang, W. Yang and J. Feng, *Adv. Mater.*, 2013, **25**, 2980–2983.
13 U. G. K. Wegst, H. Bai, E. Saiz, A. P. Tomsia and R. O. Ritchie, *Nat. Mater.*, 2015, **14**, 23–36.
14 P. Podsiadlo, A. K. Kaushik, E. M. Arruda, A. M. Waas, B. S. Shim, J. D. Xu, H. Nandivada, B. G. Pumplin, J. Lahann, A. Ramamoorthy and N. A. Kotov, *Science*, 2007, **318**, 80–83.
15 H.-B. Yao, H.-Y. Fang, X.-H. Wang and S.-H. Yu, *Chem. Soc. Rev.*, 2011, **40**, 3764–3785.
16 J. Wang, Q. Cheng and Z. Tang, *Chem. Soc. Rev.*, 2012, **41**, 1111–1129.
17 Z. Tai, J. Yang, Y. Qi, X. Yan and Q. Xue, *RSC Adv.*, 2013, **3**, 12751–12757.
18 S. Pei, J. Zhao, J. Du, W. Ren and H.-M. Cheng, *Carbon*, 2010, **48**, 4466–4474.
19 I. K. Moon, J. Lee, R. S. Ruoff and H. Lee, *Nat. Commun.*, 2010, **1**, 1067.
20 W. Cui, M. Li, J. Liu, B. Wang, C. Zhang, L. Jiang and Q. Cheng, *ACS Nano*, 2014, **8**, 9511–9517.
21 Q. Cheng, M. Wu, M. Li, L. Jiang and Z. Tang, *Angew. Chem., Int. Ed.*, 2013, **52**, 3750–3755.
22 N. V. Medhekar, A. Ramasubramaniam, R. S. Ruoff and V. B. Shenoy, *ACS Nano*, 2010, **4**, 2300–2306.
23 O. C. Compton, S. W. Cranford, K. W. Putz, Z. An, L. C. Brinson, M. J. Buehler and S. T. Nguyen, *ACS Nano*, 2012, **6**, 2008–2019.
24 K. Hu, L. S. Tolentino, D. D. Kulkarni, C. Ye, S. Kumar and V. V. Tsukruk, *Angew. Chem., Int. Ed.*, 2013, **52**, 13784–13788.
25 M. Zhang, L. Huang, J. Chen, C. Li and G. Shi, *Adv. Mater.*, 2014, **26**, 7588–7592.
26 S. Wan, J. Peng, Y. Li, H. Hu, L. Jiang and Q. Cheng, *ACS Nano*, 2015, **9**, 9830–9836.
27 R. Xiong, K. Hu, A. M. Grant, R. Ma, W. Xu, C. Lu, X. Zhang and V. V. Tsukruk, *Adv. Mater.*, 2015, DOI: 10.1002/adma.201504438.
28 S. Wan, Y. Li, J. Peng, H. Hu, Q. Cheng and L. Jiang, *ACS Nano*, 2015, **9**, 708–714.
29 S. Gong, W. Cui, Q. Zhang, A. Cao, L. Jiang and Q. Cheng, *ACS Nano*, 2015, **9**, 11568–11573.